 Q. J. R. Meteorol. Soc. 140: 1756–1770, July 2014 A DOI:10.1002/qj.2261

RMetS
Royal Meteorological Society

Tropical convection: the effects of ambient vertical and horizontal vorticity

Gerard Kilroy, Roger K. Smith*and Ulrike Wissmeier
Meteorological Institute, Ludwig-Maximilians University of Munich, Germany

*Correspondence to: R. K. Smith, Meteorological Institute, Ludwig-Maximilians University of Munich, Theresienstr. 37, 80333 Munich, Germany. E-mail: roger.smith@lmu.de

We present a series of idealized numerical model experiments to investigate aspects of deep convection in tropical depressions, including the effects of boundary-layer wind structure on storm structure, especially on vertical vorticity production and updraught splitting, and the combined effects of horizontal and vertical shear on vertical vorticity production, with and without background rotation.

In warm-cored disturbances such as tropical depressions, the vertical shear and horizontal vorticity change sign at some level near the top of the boundary layer so that, unlike in the typical middle-latitude 'supercell' storm, the tilting of horizontal vorticity by a convective updraught leads not only to dipole patterns of vertical vorticity, but to a reversal also in sign of the updraught rotation with height. This finding has implications for understanding the merger of convectively induced vorticity anomalies during vortex evolution. Ambient cyclonic horizontal shear and/or cyclonic vertical vorticity favour amplification of the cyclonically rotating gyre of the dipole.

Consistent with an earlier study, storm splitting occurs in environments with pure horizontal shear as well as pure vertical shear, but the morphology of splitting is different. In both situations, splitting is found to require a relatively unstable sounding and relatively strong wind shear.

Key Words: tropical cyclone; tropical cyclogenesis; vortical hot towers; vortical deep convection; split storms; rotating updraughts

Received 28 February 2013; Revised 27 August 2013; Accepted 29 September 2013; Published online in Wiley Online Library 14 February 2014

1. Introduction

Three-dimensional numerical model simulations of tropical cyclogenesis and tropical cyclone intensification have shown that deep convection growing in environments with enhanced levels of background rotation has a distinctive vortical structure (Hendricks *et al.*, 2004; Montgomery *et al.*, 2006; Nguyen *et al.*, 2008, 2010; Shin and Smith, 2008; Fang and Zhang, 2010; Gopalakrishnan *et al.*, 2011; Bao *et al.*, 2012; Persing *et al.*, 2013). Typically, the vertical vorticity in the convective updraughts is between one and two orders of magnitude larger than that in the immediate updraught environment, raising the possibility that updraught rotation may be an important aspect of the dynamics of these vortices. In fact, the simulations indicate that the patches of cyclonic vorticity produced by updraughts grow horizontally in scale due to mergers and axisymmetrization with neighbouring patches, leading ultimately to a vortex-scale monopole of cyclonic vorticity.

The foregoing discoveries have motivated efforts to document vortical updraughts in observations of tropical cyclones. A summary of these efforts is given by Wissmeier and Smith (2011, section 1.2). Further, recognition of the possible important role of cloud rotation on the dynamics of tropical cyclogenesis and tropical cyclone intensification has led to a few studies of the effects of *ambient vertical vorticity* on the dynamics of deep convection in isolation (Rozoff, 2007; Wissmeier and Smith, 2011; Kilroy and Smith, 2012).

There have been numerous previous numerical studies of the effects of an ambient *vertical* wind shear on convection, mostly in the context of severe convective storms in the middle latitudes (Schlesinger, 1978; Weisman and Klemp, 1982, 1984; Rotunno and Klemp, 1985; Gilmore *et al.*, 2004; see section 8.8.3 of Cotton *et al.*, 2011, for a recent review and additional references). It is pertinent to review the main results of these early studies briefly to provide a context for more recent studies of convection growing in an environment with vertical vorticity.

1.1. Storm growth in vertical shear

A considerable focus in studies of severe convective storms has been on the phenomenon of storm splitting. Typically, in the presence of horizontal vorticity associated with vertical shear, the first cell of convection generates a dipole of vertical vorticity within it. As it becomes loaded with water condensate, a downdraught

forms and develops into a cold-air outflow. Triggered by lifting at the leading edge of this outflow, subsequent cells of convection form within the positive and negative regions of the vorticity dipole and amplify the vorticity by stretching to form a pair of counter-rotating updraughts (Wilhelmson and Klemp, 1978, 1981; Weisman and Klemp, 1982; Rotunno and Klemp, 1982, 1985). If the broad-scale wind veers with height, the cyclonically rotating cell tends to be stronger than the anticyclonic one, while the anticyclonic cell is favoured when the broad-scale wind backs with height (Schlesinger, 1978; Rotunno and Klemp, 1982). This mechanism has been shown to be important in the generation of so-called 'supercell thunderstorms', first described by Browning (1964). The occurrence of storm splitting and supercell storms is favoured by large low-level vertical shear and large instability as characterized by the Convective Available Potential Energy (CAPE: Schlesinger, 1978; Wilhelmson and Klemp, 1978). Typical values of vertical wind shear in cases where splitting occurs in models is on the order of $10-20\,\mathrm{m\,s^{-1}}$ across the lowest 2–4 km, with typical values of CAPE being on the order of $2000\,\mathrm{J\,kg^{-1}}$ (Wilhelmson and Klemp, 1978; Rozoff, 2007).

Wilhelmson and Klemp (1978) suggested that low-level shear is more important than upper-level shear to the development of supercell storms, both in models and reality. Pursuing this suggestion, Weisman and Klemp (1982) investigated a unidirectional wind profile with positive vertical shear from the surface to a height of 4 km. They found that an increase in the magnitude of the shear leads to a decrease in the strength of the updraught and the vertical vorticity produced by stretching, but an increase in that produced by tilting. They showed also that, in cases of split storms, the vorticity extrema are larger in magnitude after splitting has occurred than in the vortex couplet produced by the initial cell. Up to a point, the magnitude of vorticity increases with increasing shear, but subsequent increases in shear inhibit early storm growth and hence the strength of the vorticity dipole.

1.2. *Storm growth with ambient vertical vorticity*

Rozoff (2007) carried out a series of idealized numerical model simulations on an f-plane to explore the effects of uniform horizontal shear, uniform vertical shear and a combination of both horizontal and vertical shear on the evolution of deep convection. He found that storm splitting occurs in all cases (pure vertical shear, pure horizontal shear or a combination thereof), provided that the shear is sufficiently large. With pure vertical shear, splitting occurs by the classical mechanism described above. With pure horizontal shear, splitting occurs because the initial thermal bubble is progressively elongated by the shear as it rises. Subsequently, a pair of deep convective cells develops near the tips of this elongated thermal. The vorticity enhancement in these cells is due to the stretching of ambient vertical vorticity and therefore both cells have the same sense of rotation. In the case of horizontal and vertical shear, the outcome depends on the relative magnitude of the effects for pure vertical shear and pure horizontal shear. Rozoff showed, *inter alia*, that horizontal shear is generally detrimental to the development of convection and quantified the effect of different amounts of shear on the strength and structure of the convection. *We show herein that the mechanism articulated by Rozoff involving pure horizontal shear is dependent on the initial thermal bubble being of sufficient horizontal extent and on the characteristics of the environmental sounding.*

Wissmeier and Smith (2011) described also a series of idealized numerical model experiments designed to isolate and quantify the influence of ambient vertical vorticity on the dynamics of deep convection, such as that in a tropical depression.[†] The vertical vorticity was represented by either a uniform *horizontal* shear, a uniform solid-body rotation or a combination of both. As in the studies discussed above, they found, *inter alia*, that the growing convective cells amplify the ambient vorticity locally at low levels by more than an order of magnitude and that this vorticity, which is produced by the stretching of existing ambient vorticity, persists long after the initial updraught has decayed. They found also that significant amplification of vorticity occurs even for a background rotation rate typical of the undisturbed tropical atmosphere and even for clouds of only moderate vertical extent. The simulations ignored several processes that are likely to be important in reality, such as ambient vertical shear and surface friction, but they represent benchmark calculations for interpreting the additional complexity arising from the inclusion of these effects. Kilroy and Smith (2012) used the same model as Wissmeier and Smith to examine the effects of dry ambient air on vorticity production by moderate and deep convection, again in the absence of vertical shear.

1.3. *Convective environments in tropical cyclones*

In the classical middle-latitude thunderstorm environment, the ambient wind increases in strength with height and the horizontal vorticity has a single sign from the surface upwards. However, in tropical depressions, the tangential wind speed decreases with height above a shallow boundary layer so that the sign of the radial vorticity component changes sign at some low level, typically on the order of 1 km. In contrast, the radial wind component may increase or decrease with height at low levels, depending on the radius (see e.g. Smith and Montgomery, 2013). In addition, levels of ambient absolute vertical vorticity may be much larger than in middle-latitude thunderstorm environments. Thus, deep convection that develops in tropical cyclones may have a significantly different morphology from convection that develops in middle latitudes, a fact that motivates one aspect of the present work. To our knowledge there have been no numerical studies of convection performed with a wind profile as described above. A key question that we address here is: how does this wind structure affect the generation of vertical vorticity and its vertical structure?

1.4. *The present study*

One aim of the present study is to extend the work of Wissmeier and Smith (2011) by investigating and quantifying the combined effects of both horizontal and vertical wind shear on deep convection that develops in a thermodynamic environment typical of a tropical depression. Particular attention is focused on the generation of vertical vorticity by convection and the role of boundary-layer shear. A second aim is to examine the role of a deep layer of negative vertical shear overlying a shallow layer of positive vertical shear on storm morphology. This pattern of shear arises in the tangential wind direction in tropical cyclones, although the complete boundary-layer flow in a tropical cyclone is not unidirectional. A third aim of the article is to re-examine the mechanisms involved in storm splitting discussed by Rozoff (2007), again giving particular attention to vertical vorticity generation. Since there is observational evidence for the occurrence of supercell convection in tropical storms (e.g. Gentry *et al.*, 1970; Black, 1983), one may presume that storm splitting is a relevant process in these systems also.

The article is organized as follows. In section 2 we give a brief description of the numerical model and the configuration of the experiments. The results of experiments performed with purely

[†]The current website of the Hurricane Research Division (http://www.aoml.noaa.gov/hrd/tcfaq/A1.html) uses 'tropical cyclone' as the generic term for a non-frontal synoptic-scale low-pressure system over tropical or subtropical waters with organized convection (i.e. thunderstorm activity) and a definite cyclonic surface wind circulation. Notably, this definition does not invoke any wind threshold. The same glossary defines a tropical depression as a tropical cyclone with maximum sustained surface winds of less than $17\,\mathrm{m\,s^{-1}}$ (34 knot, 39 mph) and, in the Atlantic and Eastern Pacific Basins, a 'tropical storm' as a tropical cyclone with surface winds between 17 and $33\,\mathrm{m\,s^{-1}}$.

vertical shear are presented in section 3. In sections 4 and 5 we investigate storm splitting in experiments with a background of pure vertical shear and pure horizontal shear, respectively. The effects of combined horizontal and vertical shear are examined in sections 6 and 7, with section 7 focusing on splitting events. The conclusions are given in section 8.

2. The numerical model

Following Wissmeier and Smith (2011) and Kilroy and Smith (2012), the numerical model used for this study is the state-of-the-art three-dimensional cloud model of Bryan and Fritsch (2002) and Bryan (2002). The model retains several terms in the governing thermodynamic and pressure equations that are often neglected in atmospheric models: in particular, the model accounts for the heat content of hydrometeors (Bryan and Fritsch, 2002). The model incorporates a parametrization scheme for warm rain processes as well as one for processes involving ice microphysics. The latter is Gilmore's Li-scheme, an adaptation of the popular Lin *et al.* (1983) scheme, in which cloud water, rain water, cloud ice, snow and hail/graupel are predicted (Gilmore *et al.*, 2004). The model has no parametrization of the planetary boundary layer. For simplicity, radiation effects are neglected and there are no surface fluxes of momentum, heat and moisture. A sixth-order horizontal advection scheme, which is not diffusive, is chosen. An additional artificial filter is applied to all variables to ensure stability using a coefficient suggested by George Bryan (personal correspondence).

2.1. Model configuration

The experiments use the same model configurations as those of Experiments 2, 3 and 8 of Wissmeier and Smith (2011), except that the horizontal grid spacing is halved to give improved horizontal resolution of the cloud updraughts. The horizontal domain size is 50 km × 50 km with a uniform horizontal grid spacing of 250 m. The vertical domain extends to a height of 28 km, with the vertical grid interval stretching smoothly from 120 m at the surface to 1000 m at the top. There are 50 grid levels in the vertical, eight of which are below 850 mb. The large time step is 3.7 s and the integration time is 2 h. There are eight small time steps per large time step to resolve fast-moving sound waves. The default 'open' boundary conditions are used at the lateral boundaries. A sponge layer is implemented in the uppermost 2 km to inhibit the reflection of gravity waves from the upper boundary. All experiments include warm rain physics, while one experiment implements an ice microphysics scheme also.

As in Wissmeier and Smith (2011), we have not sought to initialize the calculations from a geostrophically balanced state, partly because the Bryan model is not easily configured to allow this, but also because interest is confined to times much shorter than the inertial period ($\mathcal{O}$(6 h)).

2.2. The numerical experiments

We describe a total of ten numerical experiments, details of which are summarized and compared in Table 1. The first three experiments examine the role of pure vertical shear in a configuration typical of the tangential wind structure of a tropical depression. The fourth experiment examines the role of pure horizontal shear on deep convection in a tropical depression, while the remaining experiments investigate the combined effects of horizontal and vertical shear in such a disturbance. Further details about the experiments and their objectives are given in the relevant sections.

2.3. Background wind profiles

In all experiments, the background flow is in the meridional (y-) direction of a rectangular Cartesian coordinate system, (x, y, z), with z pointing vertically upwards. The background wind profiles for Experiments 1–3 have vertical shear only and are shown in Figure 1. The profiles are given by the formula

$$V(z) = \begin{cases} V_s + (V_m - V_s)\sin\left(\dfrac{\pi z}{2h}\right) & \text{for } z \le h \\ V_m \cos\left(\dfrac{\pi(z-h)}{2H}\right) & \text{for } z \ge h\,, \end{cases} \quad (1)$$

where V_m is 20 m s^{-1}, $H = 15$ km and other parameters differ between experiments. Above 15 km, the wind speed is set to zero. In Experiment 1, $h = 0$, giving the maximum wind speed at the surface. In this case, only the cosine profile applies and the wind profile has negative vertical shear at all heights. In Experiment 2, $h = 1$ km and $V_s = 0.7V_m$. In this case, the cosine profile applies above a height of 1 km and the sine profile below to represent a boundary layer with positive vertical shear. Experiment 3 is similar to Experiment 2, but has $V_s = 0.5V_m$ and therefore a larger positive shear in the boundary layer.

The background wind profile for Experiment 4 is given by the formula

$$V(x) = 3\zeta_o x, \quad (2)$$

where $\zeta_o = 3 \times 10^{-4}$ s^{-1}, the value used by Wissmeier and Smith (2011, section 2.3) as 'typical' of that in a tropical depression (e.g. Foster and Lyons, 1984; Douglas, 1992), with the caveat that vorticity may vary considerably with radius in any vortex.

The background wind profile for Experiments 5–10 is shown in Figure 2. This idealized profile is chosen to extend the results of Wissmeier and Smith (2011) and is given by the formula

$$V(x, z) = V_o(x)[1 - b\exp(-az)], \quad (3)$$

Table 1. Details of the ten experiments studied herein.

Exp	Microphysics	Horizontal shear	f	Vertical shear	Sounding
1	Warm rain	None	0	No BL profile	Standard
2	Warm rain	None	0	BL profile	Standard
3	Warm rain	None	0	BL profile*	Unstable
4	Warm rain	$3\zeta_o$	0	None	Unstable
5	Warm rain	ζ_o	0	Standard	Standard
6	Warm rain	ζ_o	$\frac{1}{2}\zeta_o$	Standard	Standard
7	Warm rain	ζ_o	ζ_o	Standard	Standard
8	Rain + ice	ζ_o	0	Standard	Standard
9	Warm rain	None	0	Standard*	Unstable
10	Warm rain	ζ_o	0	Standard*	Unstable

Notes: $\zeta_0 = 3 \times 10^{-4}$ s^{-1}. (*) refers to the wind profile in Experiments 3, 9 and 10, which is altered to increase the low-level vertical shear. The equations for the different types of vertical shear are given in section 2.3. Experiments 3, 4, 9 and 10 use a different environmental sounding, which is more unstable than the standard sounding. The thermodynamic soundings are discussed in section 2.4.

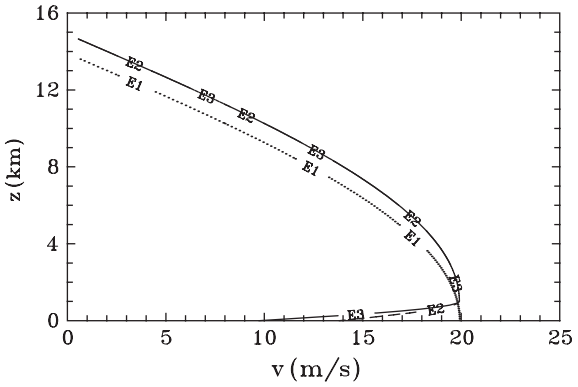

Figure 1. Schematic of the background wind field used for Experiments 1–3. The dotted curve denotes V for Experiment 1, the dashed curve V for Experiment 2 and the solid curve V for Experiment 3.

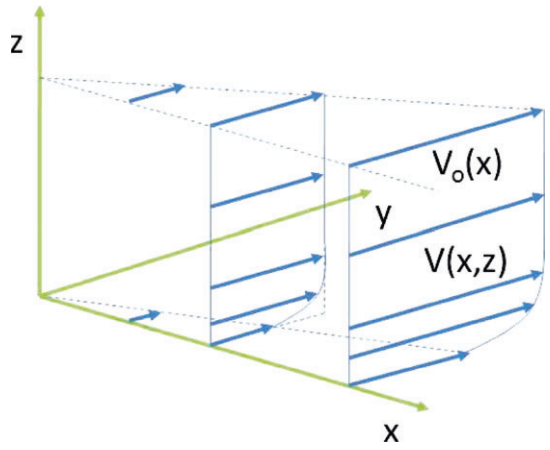

Figure 2. Schematic of the 'standard' background flow used for Experiments 5–10. The domain is 50 km × 50 km and the thermal bubble used to initiate convection is located at the centre of the domain. This figure is available in colour online at wileyonlinelibrary.com/journal/qj

where $b = 0.5$, $a = -\log(0.05/b)/2000$ m and $V_o(x) = \zeta_o x$. The wind speed increases monotonically with z from a value $0.5V_o(x)$ at the surface, reaching 95% of V_o at a height of 2 km. For simplicity, above this height the wind has essentially uniform horizontal shear only.

A uniform flow is added to the wind profile in all experiments to keep the convection near the centre of the computational domain. The value of this flow is determined by trial and error and is different for each experiment.

2.4. *Thermodynamic soundings*

Experiments 1–2 and 5–8 use the idealized thermodynamic sounding shown in Figure 3(a). This sounding is similar to that used in Experiment 1 of Kilroy and Smith (2012), with piecewise-linear profiles of virtual potential temperature, θ_v, and mixing ratio, r, but it is slightly drier at low levels. Accordingly, the Convective Available Potential Energy (CAPE) is less than that of the sounding used in Kilroy and Smith (2012) (2080 J kg^{-1} compared with 2770 J kg^{-1}). The construction of both soundings is based on an observed sounding made near the centre of the low-level circulation of ex-Tropical Storm *Gaston* on 5 September 2010 during the Pre-Depression Investigation of Cloud-systems in the Tropics (PREDICT) experiment (see Smith and Montgomery, 2012, their figure 6). This region of ex-*Gaston* was one of high total precipitable water (TPW), high CAPE[‡] and low Convective Inhibition (CIN).[§] The sounding used here has a minimum CIN of 40 J kg^{-1} and a TPW value of 59.1 kg m^{-2}. The idealized sounding has a temperature structure close to that of the mean tropical sounding of Dunion and Marron (2008), but it is moister in the lower troposphere and much drier in the upper troposphere.

A prerequisite for storm splitting is a sufficiently large low-level vertical shear. However, for a given sounding, large vertical shear tends to inhibit convection because the initial thermal becomes elongated and weakened. Therefore, in a strongly sheared environment, a particularly unstable sounding may be necessary to initiate convection. An example of such a sounding is one observed during the PREDICT experiment, which was used in Experiments 6–8 of Kilroy and Smith (2012). This sounding, shown in Figure 3(b), has moderate CAPE (1650 J kg^{-1}) but zero CIN and a TPW value of 67.1 kg m^{-2}. In Experiment 8 of Kilroy and Smith, it was possible to initiate a deep convective updraught with an initial warm temperature excess of only 0.25 K. We use this sounding in Experiments 3, 4, 9 and 10 because the CIN of the standard sounding used in the other experiments is too large for convection to be triggered at larger magnitudes of vertical shear.

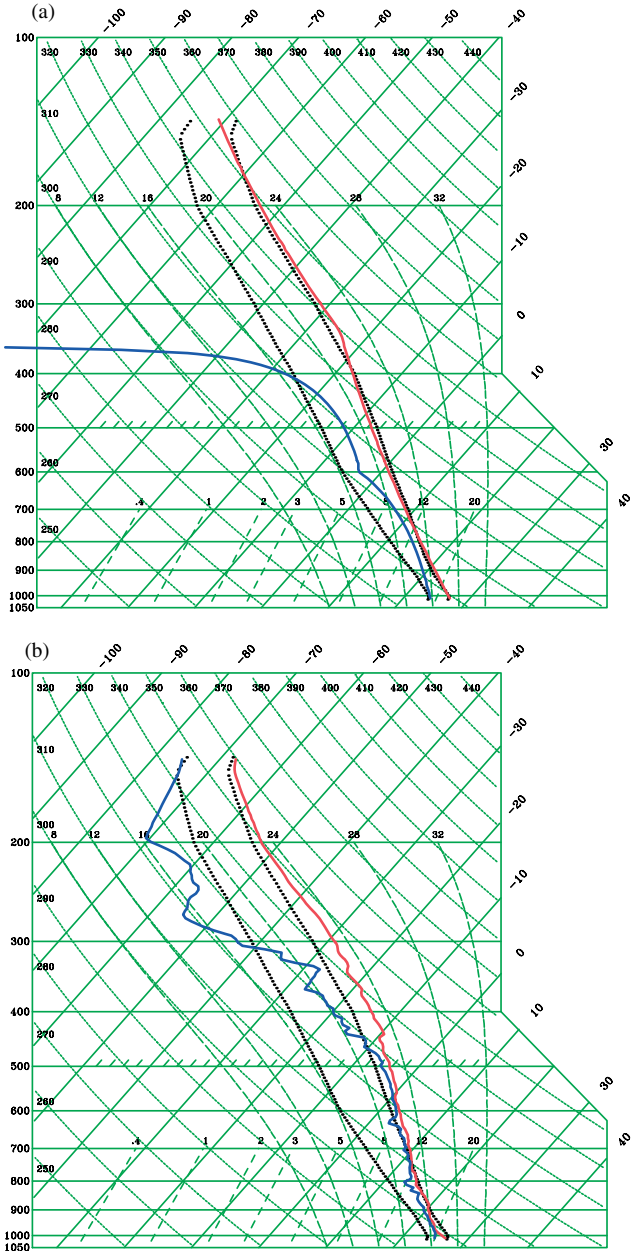

Figure 3. Skew-T–log p diagram showing the temperature (right solid curve) and dew-point temperature (left solid curve) of (a) a standard sounding and (b) the PREDICT sounding from 2 September at 1703 UTC. For comparison, the dotted curves show the temperature (right curve) and dew-point temperature (left curve) for the mean tropical sounding of Dunion and Marron (2008). This figure is available in colour online at wileyonlinelibrary.com/journal/qj

2.5. *Initiation of convection*

Convection is initiated by a symmetric thermal perturbation with a horizontal radius of 5 km and a vertical extent of 1 km as in Kilroy and Smith (2012). The temperature excess has a maximum at the surface at the centre of the perturbation and decreases monotonically to zero at the perturbation's edge. The perturbation centre coincides with the centre of the domain. In general, the details of the ensuing convection such as the

[‡]We remind the reader that CAPE is a parcel quantity that typically has a strong negative vertical gradient in the lower troposphere. For this reason, the values cited herein are based on an average for air parcels lifted from the surface and at 100 m intervals above the surface to a height of 500 m. Since the calculation of CAPE is a nonlinear function of temperature and moisture, we prefer this method to one based on averaged values of temperature and mixing ratio through a surface-based layer of air with some arbitrarily prescribed depth.

[§]Like CAPE, CIN is a quantity that refers also to an air parcel. Rather than computing an average up to 500 m as for CAPE, it seems physically more reasonable to examine the minimum value of CIN up to this level.

Table 2. Maximum vertical velocity, wN_{max}, and minimum vertical velocity, wN_{min}, at a height of N km and the times at which they occur, $t(wN_{max})$ and $t(wN_{min})$ respectively, in Experiments 1–10. The first two columns display the maximum and minimum velocities throughout the domain and the 2 h integration time.

Experiment	w_{max}	w_{min}	$w2_{max}$ ($m\,s^{-1}$)	$t(w2_{max})$ (min)	$w5_{max}$ ($m\,s^{-1}$)	$t(w5_{max})$ (min)	$w9_{max}$ ($m\,s^{-1}$)	$t(w9_{max})$ (min)	$w2_{min}$ ($m\,s^{-1}$)	$t(w2_{min})$ (min)
1	26.8	−6.9	10.8	26	25.3	30	6.1	44	−3.3	40
2	15.5	−3.3	6.2	38	14.2	48	1.0	70	−1.7	40
3	16.5	−7.8	13.2	120	15.6	110	13.2	120	−5.9	110
4	20.1	−6.8	13.6	20	16.5	26	11.5	46	−5.5	28
5	23.8	−6.4	9.4	28	21.5	34	4.5	48	−2.9	34
6	23.2	−6.6	9.6	28	20.8	34	4.7	48	−2.7	40
7	23.6	−6.4	9.6	28	21.4	34	5.3	48	−2.6	40
8	26.1	−8.3	11.4	26	23.4	30	4.5	44	−4.4	42
9	18.7	−7.6	13.6	52	16.4	114	14.9	52	−6.6	98
10	21.6	−8.1	14.8	104	17.7	102	15.3	102	−7.0	84

maximum updraught strength and the updraught depth will depend on the spatial structure and amplitude of the thermal perturbation. While this method for the initiation of convection is necessarily artificial, it is unclear how to improve upon it significantly and for this reason it has been widely used in numerical studies of deep convection (see e.g. Weisman and Klemp, 1982; Gilmore *et al.*, 2004; Rozoff, 2007; Wissmeier, 2009[¶] and Wissmeier and Smith, 2011.) A maximum temperature perturbation of 2 K is used in all experiments.

In reality, thermal perturbations over the ocean will be linked to surface heat fluxes, but there are other ways in which convection may be triggered, such as lifting at gust front boundaries generated by prior convection. We plan to examine the effects of such processes on vertical vorticity generation in a subsequent article.

3. Unidirectional vertical shear with and without a boundary-layer wind profile

Experiments 1–4 are designed as a preliminary step towards determining the combined effects of ambient horizontal and vertical shear on vertical vorticity production in tropical convection. In Experiments 1–3 we examine cases of convection developing in an environment with unidirectional vertical shear and in Experiment 4 we examine development in an environment of pure uniform *horizontal* shear, in all cases with no background rotation. In this section we discuss Experiments 1 and 2 and in sections 4 and 5 we discuss Experiments 3 and 4, respectively.

Experiment 1 serves as a control experiment: it has maximum wind speeds at the surface and a negative vertical shear from the surface to the upper troposphere, characteristic of the wind structure in a warm-cored vortex. Experiment 2 is a little more realistic and designed to investigate the additional effects of a boundary-layer wind profile where the wind speed increases with height to a maximum near a height of 1 km before declining. Therefore the horizontal vorticity changes from positive to negative at this height, which is near the top of the boundary layer. In other respects the experiment is the same as Experiment 1.

Details of the maximum updraught and downdraught strength at selected heights are given in Table 2, while those of the maximum and minimum vertical vorticity at selected heights are given in Table 3 for all experiments. The imposition of a boundary-layer wind profile has a dramatic effect on the vertical velocity: whereas, in Experiment 1, w_{max} is 26.8 $m\,s^{-1}$, in Experiment 2 it is only 15.5 $m\,s^{-1}$ (Table 2). Moreover, in Experiment 2, the updraught barely extends above a height of 9 km, the maximum vertical velocity at a height of 9 km, $w9_{max}$, being only 1 $m\,s^{-1}$ at 70 min. In addition to a much stronger updraught, the maximum downdraught strength in Experiment 1 (6.9 $m\,s^{-1}$) is more than twice that in Experiment 2 (3.3 $m\,s^{-1}$).

To help interpret the foregoing results, we performed another two experiments (results not shown in Table 2), one where the layer of positive vertical shear is confined to the lowest 500 m instead of the lowest 1 km, essentially doubling the amount of vertical shear in the lowest 500 m compared with Experiment 2. In the other experiment, the wind profile above a height of 2 km in Experiment 1 is extrapolated linearly to the surface so that the maximum wind speed occurs at the surface and there is uniform negative shear everywhere. In the first of these experiments, no convection occurred. The reason is because the increased low-level shear deforms the initial thermal bubble so that it becomes too weak to generate convection. The second of these experiments produces a similar vertical velocity maximum to that found in Experiment 2. Thus, low-level vertical shear weakens the initial thermal before convection occurs, whether or not the shear is positive or negative. The weakening depends only on the magnitude of the shear. Note that Experiment 1, which has little vertical shear in the lowest 1 km, produces the strongest updraught. The weakening of the thermal bubble by shear is confirmed by height–time plots of the maximum temperature perturbation in the different experiments at early times (not shown).

Figure 4 shows time–height cross-sections of maximum[‖] vertical vorticity in Experiments 1 and 2 and Table 3 gives details of the maxima and minima at selected heights.

In Experiment 1, the vertical gradient of V is small from the surface to around 2 km (Figure 1), whereupon there is very little horizontal vorticity available to be tilted into the vertical. This fact explains why values of vertical vorticity are weak at low levels in Figure 4(a). There is significant vertical shear above a height of 2 km so that tilting of horizontal vorticity by the updraught leads to values of vertical vorticity that are much larger. Note that $\zeta_{max} = 2.6 \times 10^{-2}\,s^{-1}$ at a height of 6.5 km (see Table 3).

In Experiment 2 there is positive vertical shear below a height of about 1 km and negative shear above. Thus, the sign of background horizontal vorticity reverses at this height and there is an elevated layer in which the magnitude of the horizontal vorticity is small and hence the vertical vorticity production by tilting is small. For this reason, there is an intermediate layer

[¶]Their section 3.4.2 examines the sensitivity of the storm's updraught strength to the width, depth and temperature excess of the warm bubble.

[‖]The evolution of the updraught associated with the rising thermal bubble is similar to that described in Wissmeier and Smith (2011) and Kilroy and Smith (2012), although the depiction here is slightly different. In the above studies there was no ambient vertical shear, so that the first convective cell was upright and axisymmetric about its central axis. This feature allowed the depiction of the evolution of updraughts and downdraughts as height–time series along this axis without ambiguity. The presence here of an ambient vertical shear means that updraughts and downdraughts are tilted so that the extrema of vertical velocity and vertical vorticity occur at different spatial locations at different times. This feature makes a single cross-section for updraught and downdraught extrema or for positive and negative vorticity inappropriate. Plots of the minimum vertical vorticity are omitted in this section because, in the absence of background rotation or horizontal wind shear, they are a mirror image of the maximum plots.

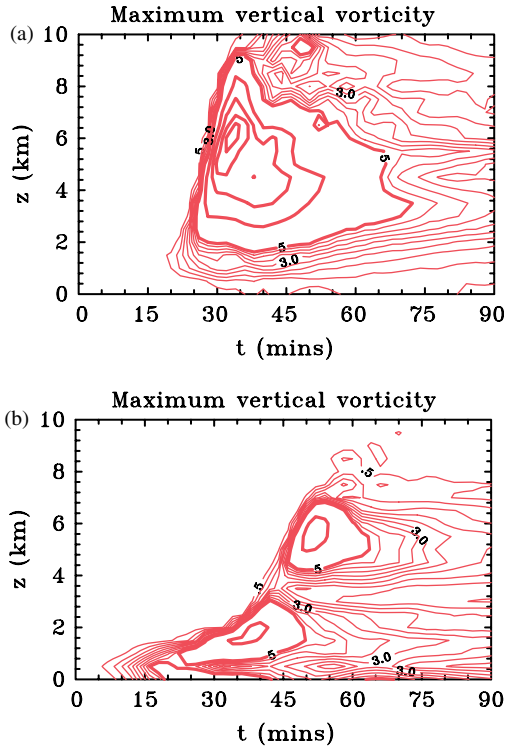

Figure 4. Time–height series of maximum vertical vorticity in (a) Experiment 1 and (b) Experiment 2. Contour interval: thin contours $0.5 \times 10^{-3}\,s^{-1}$ to $4.5 \times 10^{-3}\,s^{-1}$; thick contours $5 \times 10^{-3}\,s^{-1}$. This figure is available in colour online at wileyonlinelibrary.com/journal/qj

centred around 4 km in height with small vertical vorticity values in Figure 4(b).

Figure 5 shows horizontal cross-sections of the vertical component of relative vorticity for Experiments 1 and 2 at 30 min at a height of 1 km and at 54 min at a height of 6 km (left and middle panels). In Experiment 1, the background horizontal vorticity does not change sign with height, but the vorticity generated at low levels is much weaker than in the middle troposphere. Again this is due to the relatively small amount of background horizontal vorticity available for tilting, because of the small vertical gradient of V in the wind profile used in this experiment (compare with the low-level plot in Figure 4(a)).

Below a height of 1 km in Experiment 2, tilting by the convective updraught creates a vertical vorticity dipole with a negative vorticity anomaly to the left of the mean flow (which is in the y-direction) and a positive one to the right. Above 1 km, the vorticity dipole is reversed, with positive vorticity to the left of the flow direction and negative to the right. Figures 5(c) and (f) show y–z cross-sections of vertical velocity and vertical vorticity through the centre of the low-level positive vorticity anomaly at 52 min for Experiment 2. At this time the updraught has a maximum at a height of 6 km, but there is a region of subsidence below, centred at a height of 4 km. There are regions of subsidence also on each side of the updraught. The latter are associated with the downward branch of the rising thermal, while the downdraught centred at a height of 4 km is associated with precipitation. Panel (f) shows clearly the tilting effect of the background wind field, in which the low-level positive vorticity anomaly is tilted in the positive y-direction and the upper-level negative vorticity anomaly is tilted in the negative y-direction. The upper-level negative vorticity anomaly is relatively strong in magnitude at this time, as the minimum vorticity lies in a region of strong divergence between the updraught and downdraught. The vorticity structure in y–z through the low-level negative vorticity anomaly is the same as that in Figure 5(f), but with the sign of vorticity reversed (not shown). These findings introduce an element of complication in interpretations of the merger of convectively induced cyclonic vorticity anomalies in terms of barotropic dynamics (e.g. Nguyen *et al.*, 2008). A recent analysis of convective structures in the principal rain band of Hurricane *Rita* (2005) by Didlake and Houze (2011; their figure 8 and 9) shows slanting patterns of vertical vorticity with alternating sign. Didlake and Houze speculate that these patterns may be a result of vortex Rossby waves. However, the mechanisms described above might provide an alternative interpretation, as the updraughts occur in regimes where the vertical shear presumably changes sign with height.

The low-level shear in Experiment 2 causes the initial thermal to spread out horizontally and weaken, leading to a spatially larger convective cell at low levels. However, at upper levels the updraught is weaker than in Experiment 1 and smaller in cross-section. For this reason the generation of vorticity is weaker and the vorticity anomalies are smaller in horizontal cross-section (see Figure 5 and Table 2).

In line with vertical velocity values, the vertical vorticity is much larger in Experiment 1, where $\zeta_{max} = 2.6 \times 10^{-2}\,s^{-1}$, than in Experiment 2, where $\zeta_{max} = 1.2 \times 10^{-2}\,s^{-1}$. In both experiments, ζ_{max} occurs at a height of 6–6.5 km. These two experiments have no ambient vertical vorticity so that, initially, vertical vorticity is generated only by the tilting of horizontal vorticity into the vertical. However, once some vertical vorticity has been produced, it can be further amplified by stretching. In the absence of background vorticity, the positive and negative vortical structures that develop are symmetric and equal in strength, with neither member of the dipole strengthened more than the other, as confirmed by the identical magnitudes of ζ_{max} and ζ_{min} at heights of 1 and 4 km (Table 3).

In summary, the imposition of a boundary-layer wind profile has a dramatic effect on convection, markedly weakening convective updraughts and downdraughts, thereby reducing the amplification of vertical vorticity and lowering the height to which updraughts penetrate. The weakening results largely from the deformation of the initial bubble by the low-level vertical shear.

Table 3. Maximum of the vertical component of relative vorticity, ζN_{max}, at heights N of 500 m, 1 and 4 km and the times at which they occur, $t(\zeta N_{max})$, in Experiments 1–10. Also shown are the minima of this vorticity component at heights of 1 and 4 km, together with the times at which they occur.

Experiment	ζ_{max} ($10^{-3}\,s^{-1}$)	$z(\zeta_{max})$ (km)	$\zeta 0.5_{max}$ ($10^{-3}\,s^{-1}$)	$t(\zeta 0.5_{max})$ (min)	$\zeta 1_{max}$ ($10^{-3}\,s^{-1}$)	$t(\zeta 1_{max})$ (min)	$\zeta 4_{max}$ ($10^{-3}\,s^{-1}$)	$t(\zeta 4_{max})$ (min)	$\zeta 1_{min}$ ($10^{-3}\,s^{-1}$)	$t(\zeta 1_{min})$ (min)	$\zeta 4_{min}$ ($10^{-3}\,s^{-1}$)	$t(\zeta 4_{min})$ (min)
1	26.2	6.5	1.0	40	2.9	34	18.9	42	−2.9	34	−18.9	42
2	12.2	6.0	5.6	20	8.1	34	3.6	54	−8.1	34	−3.6	54
3	39.4	8.0	22.4	46	29.3	56	31.9	104	−29.3	56	−31.9	104
4	32.7	7.0	24.8	22	23.4	24	20.5	72	−13.7	74	−29.5	40
5	20.0	3.5	8.6	24	12.2	30	19.9	32	−11.5	30	−23.4	32
6	21.6	4.0	13.1	22	14.6	30	21.6	32	−9.4	28	−19.9	32
7	24.0	0.0	15.2	24	17.6	28	20.0	32	−8.2	28	−19.6	32
8	22.2	4.5	10.6	22	11.9	26	21.2	30	−11.9	44	−27.2	30
9	35.2	1.5	19.5	85	28.2	60	31.0	34	−28.2	60	−31.0	34
10	37.5	4.0	19.3	26	27.3	56	37.5	90	−30.8	46	−34.7	110

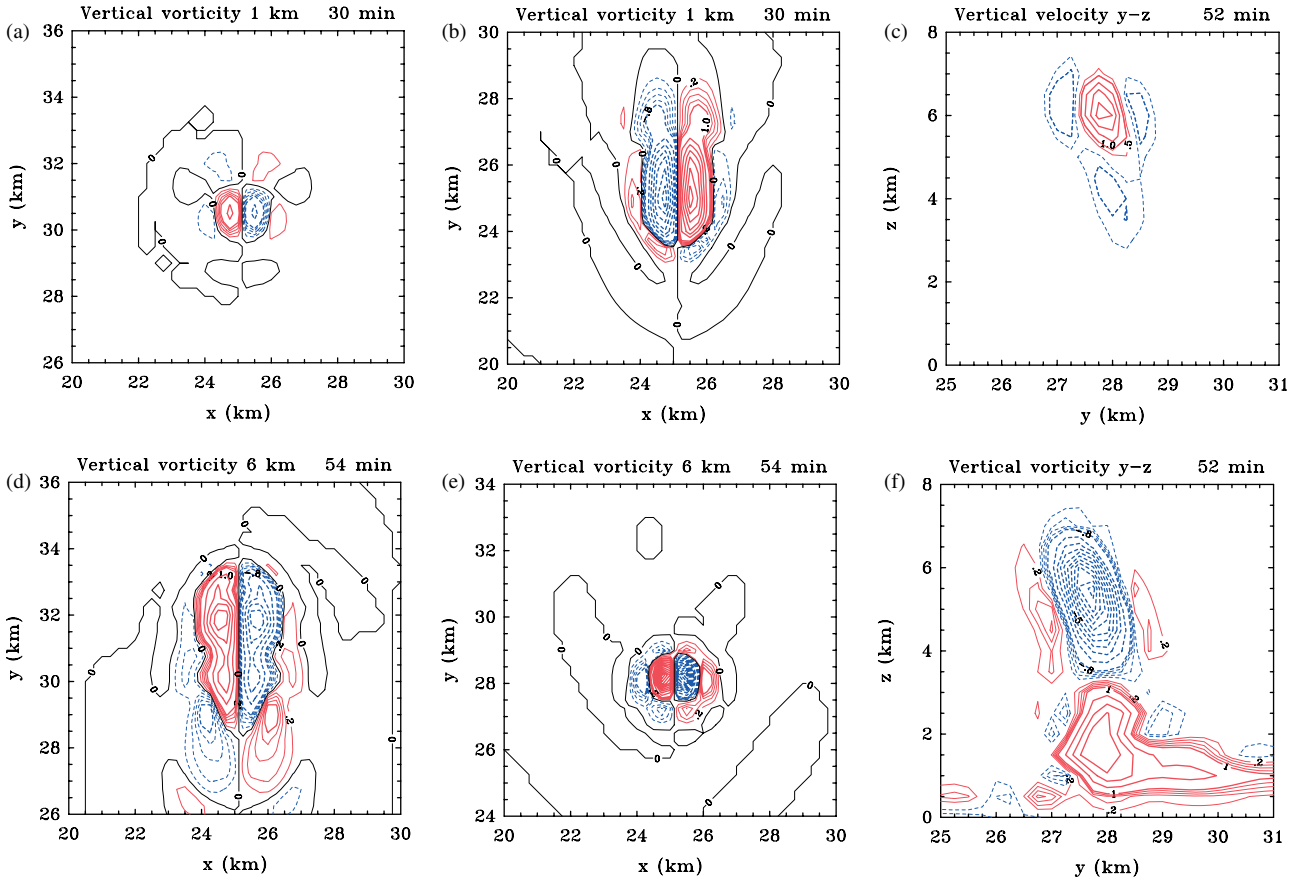

Figure 5. Horizontal cross-sections of vertical vorticity in Experiment 1 (left) and Experiment 2 (middle) at (a) and (b) 30 min at a height of 1 km and (d) and (e) 54 min at a height of 6 km. Contour interval: thin contours $2 \times 10^{-4}\,s^{-1}$ to $8 \times 10^{-4}\,s^{-1}$; thick contours $1 \times 10^{-3}\,s^{-1}$. Solid (red) contours are positive, dashed (blue) contours negative. The thin black curve shows the zero contour. The remaining panels show vertical cross-sections (y–z) at 52 min for Experiment 2 of (c) vertical velocity and (f) vertical vorticity, through the centre of the low-level positive vorticity anomaly. Contour interval: vertical velocity thin contours $0.5\,m\,s^{-1}$, thick contours $1\,m\,s^{-1}$; vertical vorticity thin contours $2 \times 10^{-4}\,s^{-1}$ to $8 \times 10^{-4}\,s^{-1}$, thick contours $1 \times 10^{-3}\,s^{-1}$. Solid (red) contours are positive, dashed (blue) contours negative. This figure is available in colour online at wileyonlinelibrary.com/journal/qj

4. Storm splitting in a pure vertical shear

Experiments 3 and 4 are designed to investigate storm splitting in an idealized vortex environment, the former in pure vertical shear and the latter in pure horizontal shear. Because of its effect in distorting the initial thermal, vertical wind shear has a detrimental effect on convective initiation in our experiments for a given thermodynamic sounding. Indeed, in an early experiment with vertical shear and the relatively stable sounding of Experiments 1 and 2, convection does not occur (results not shown). For this reason, Experiment 3 uses the more unstable sounding discussed in section 2.4. Even ignoring the additional complexities of the strong radial wind component in the boundary layer of a tropical cyclone, the results of section 3 show that a change in sign of the vertical shear implies a change in sign at some height of the vertical vorticity dipole produced by the updraught. To our knowledge, the consequences of the change of sign of this dipole for the vorticity structure of successive updraughts in the case of a split storm have not been discussed previously in the literature. Experiment 3 is designed to examine this issue.

Since storm splitting is known to occur in midlatitude storms in a regime of high vertical wind shear at low levels, Experiment 3 uses the same wind profile as Experiment 2, but with a smaller surface wind speed and therefore a larger magnitude of vertical wind shear in the boundary layer. Figure 6 shows the pattern of vertical vorticity in horizontal cross-sections at selected times at heights of 4 km (left panels) and 8 km (right panels) for this experiment. At a height of 4 km, a split develops between 44 and 70 min (Figure 6(a) and (c)), with a patch of cyclonic vorticity moving from the domain centre to the right of the mean wind and an anticyclonic patch moving to the left. At a height of 8 km, the sign of each vorticity patch is reversed, with a large positive anomaly on the left of the ordinate and a large negative anomaly on the right. These vorticity patterns are similar to those of Experiment 2, although they are more complex because new convective cells are repeatedly initiated in the more unstable environment. This pattern of reversing vorticity with height in the split cells is different from the classical updraught structure of midlatitude storms.

A notable feature of this simulation is that the domain maximum updraught and downdraught velocities occur late in the simulation, after 110 min (Table 2), and unlike the values in Experiments 1 and 2, are not representative of the initial cell. Thus the strongest vertical motion, and with it, the largest value of vertical vorticity, occurs *after storm splitting*. With the more unstable sounding and the larger low-level vertical shear compared with the configuration of Experiment 2, the maximum vertical vorticity ($3.9 \times 10^{-2}\,s^{-1}$) is more than three times as large as in Experiment 2, but like Experiment 2, this maximum occurs in the upper troposphere (above 6 km).

5. Storm splitting in a pure horizontal shear

Experiment 4 is similar to Experiment 2 of Wissmeier and Smith (2011), but has a uniform, cyclonic, horizontal shear that is three times as large, sufficient to instigate storm splitting in this configuration. Horizontal cross-sections of various quantities in this experiment are shown in Figure 7 at selected times. These include the vertical vorticity at a height of 1 km (upper panels), cloud and rain water at a height of 4 km (middle panels) and contours of vertical velocity at a height of 4 km superimposed on surface wind vectors (lower panels). By 24 min (left panels), the cloud and rain water contours and the vertical velocity contours are still relatively axisymmetric, but the vertical vorticity

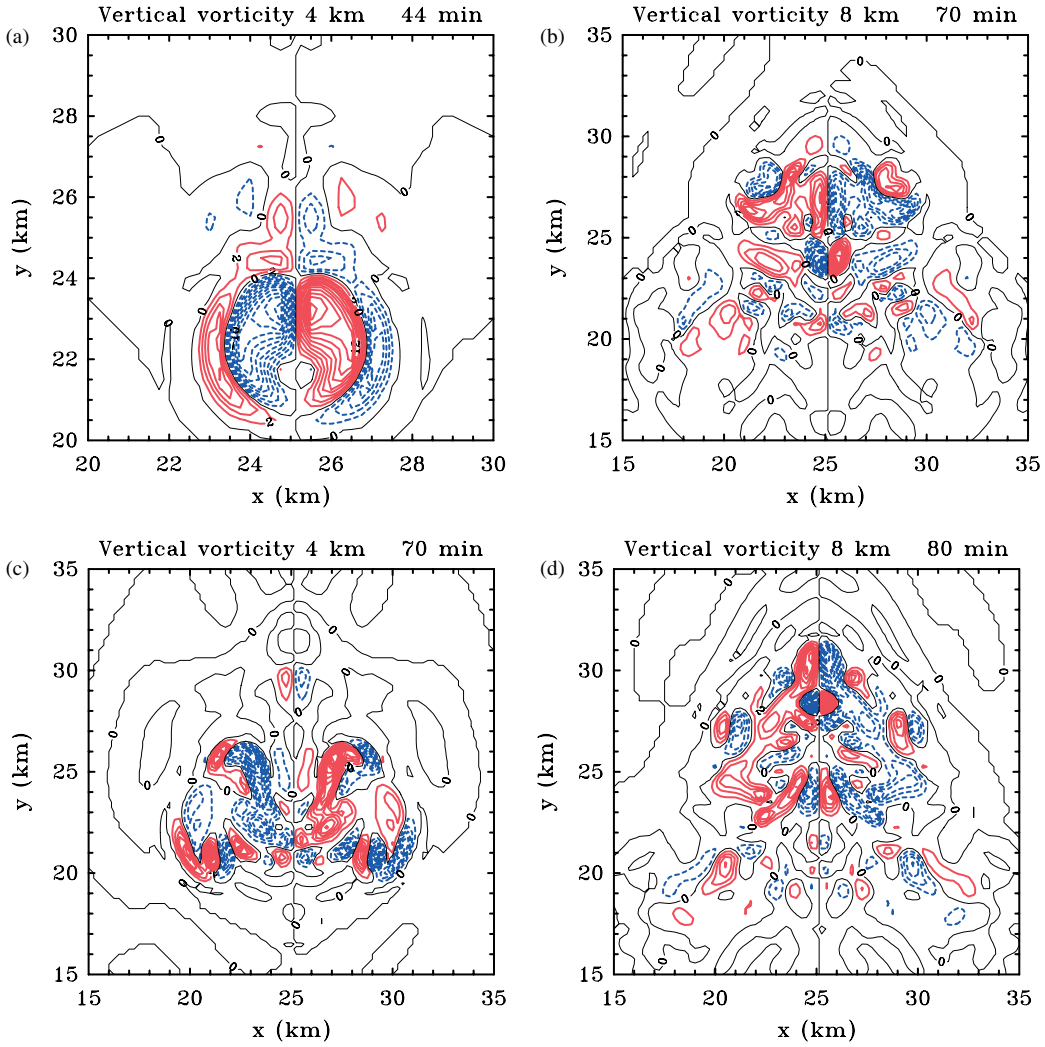

Figure 6. Horizontal cross-section of the vertical vorticity at heights of 4 and 8 km in Experiment 3 at chosen times: (a) 4 km at 44 min; (b) 8 km at 70 min; (c) 4 km at 70 min; and (d) 8 km at 80 min. Contour interval: 2×10^{-3} s^{-1}. Solid (red) contours are positive, dashed (blue) contours negative. The thin black curve shows the zero contour. This figure is available in colour online at wileyonlinelibrary.com/journal/qj

fields show the effects of the background horizontal shear. By 34 min a split is evident in the vertical velocity field and by 60 min the two updraughts are separated by approximately 10 km. At this time a large patch of positive vorticity remains where the original cell developed. There is a vorticity dipole structure also: this is associated with both the northward and southward moving cells. Interestingly, the vertical vorticity minima at heights of 1 and 4 km for Experiment 4 have values of -1.4×10^{-2} and -3.0×10^{-2} s^{-1}, respectively (both are stronger in magnitude than the vorticity maximum in Experiment 2). Thus, an appreciable *negative vorticity* anomaly is generated, even when the initial background vorticity is purely cyclonic. This negative vorticity is produced by the tilting of horizontal vorticity associated with the cold air outflow from the initial cell. The tilting is produced by the split updraughts that move over the cold pool and subsequently amplify the vertical vorticity by stretching. Because the background rotation is cyclonic, the cyclonic vorticity anomaly of the dipole is stronger in magnitude than the anticyclonic one.

The maximum updraught and downdraught strengths in Experiment 4 are 20.1 and 6.8 m s^{-1}, respectively, and they occur *before the initial cell splits*. The domain-maximum vertical vorticity in Experiment 4 is 3.3×10^{-2} s^{-1} at a height of 7 km. The vorticity maxima at heights of 500 m and 1 km occur before splitting, while the maximum at a height of 4 km occurs afterwards. This behaviour for pure horizontal shear is different from that of pure vertical shear, where the maxima of all these quantities occur after splitting.

As far as we are aware, the only previous study of storm splitting in horizontal shear is that of Rozoff (2007) and it is appropriate to compare the results of this section with his. Besides the different models used, there are two main differences between the experimental configuration in our study and in his. First, the largest value of horizontal shear used by Rozoff (2007) is -6×10^{-4} s^{-1}, while we use 9×10^{-4} s^{-1} in Experiment 4. Second, there are differences between the initial thermal bubbles. His bubble has a horizontal radius of 27.5 km, which is larger than our entire domain. Moreover, his temperature perturbation of 2 K is built up gradually over the first 200 s, while in our case it is imposed at the initial instant. In a regime of strong horizontal shear, the thermal perturbation becomes progressively elongated and the gradual addition of incremental temperature perturbations over a time period of 200 s can be expected to increase the horizontal extent of the perturbation further.

To examine the consequences of the differences between the formulation of the thermal bubble, we performed two more horizontal shear experiments with different initial bubble configurations, both of which use the more stable standard sounding (results not shown). In the first experiment, we used our initial thermal bubble and the more stable sounding and found that cell splitting *does not occur*; rather convection evolves as described in Wissmeier and Smith (2011). We repeated this experiment with an initial thermal, almost identical in size, position and temperature excess to that used by Rozoff. In this experiment, *splitting does occur with the more stable sounding*. It turns out that, as the spatial extent of the initial thermal is increased, the local buoyancy near the thermal centre (which is

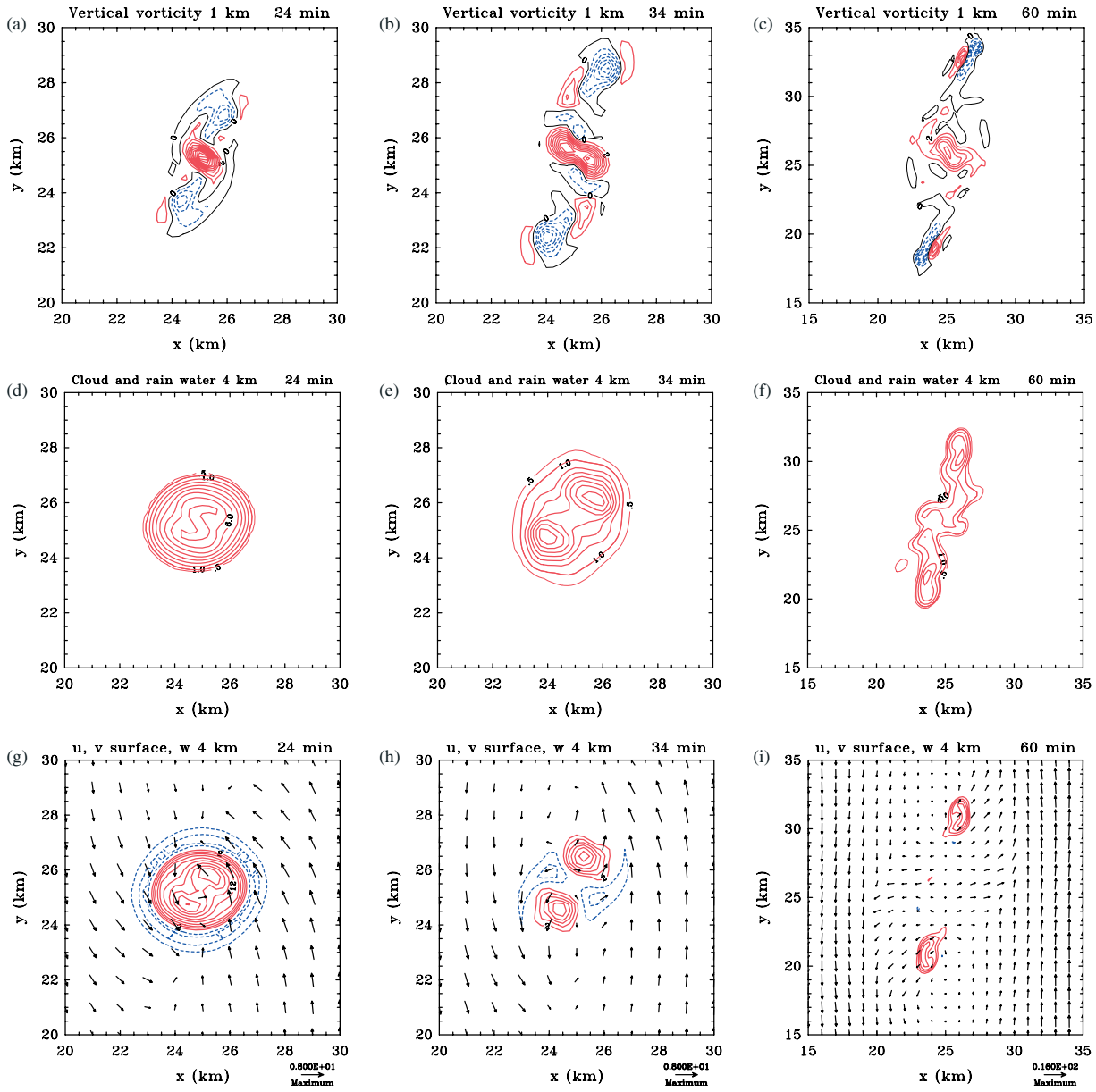

Figure 7. Horizontal cross-section of ((a)-(c)) the vertical vorticity at a height of 1 km, ((d)-(f)) cloud and rain water at a height of 4 km and ((g)-(i)) vertical velocity at a height of 4 km overlying surface wind vectors for Experiment 4 at chosen times. Contour interval: vertical vorticity contours 2×10^{-3} s^{-1}; rain and cloud water contours: thin contour 0.5 g kg^{-1} and thick contours 1 g kg^{-1}; vertical velocity contours 2 m s^{-1}, surface wind vectors are relative to the maximum vector at the bottom right of panels (g), (h) and (i). Note that the maximum vector is different in plot (i). Solid (red) contours are positive, dashed (blue) contours negative. The thin black curve shows the zero contour. This figure is available in colour online at wileyonlinelibrary.com/journal/qj

located at the domain centre) is reduced, so that convection does not occur as quickly as that initiated with a bubble of smaller horizontal scale. The delayed development allows the background horizontal shear to elongate the thermal before convective cells form at its longitudinal ends.

6. Combined horizontal and vertical shear

We consider now Experiments 5–8, which are similar to Experiments 2, 3, 5 and 8 of Wissmeier and Smith (2011), respectively, but have a different thermodynamic sounding and include also vertical shear. Experiments 6 and 7 are carried out on an f-plane, the former with Coriolis parameter $f = 0.5\zeta_o$ and the latter with $f = \zeta_o$ (Experiments 5 and 8 have no background rotation). Experiment 8 is a repeat of Experiment 5 with a representation of ice microphysics.

6.1. *Vertical velocity*

Figure 8 shows horizontal cross-sections of vertical velocity for Experiment 5 at a height of 2 km at 28 and 34 min after the initial time. The earlier time is that at which the updraught velocity is a maximum at this level and the later time is when the downdraught is a maximum. These cross-sections are typical of those in the other experiments at similar stages of development. The annular region of downdraught surrounding the updraught core in Figure 8(a) is part of the subsiding branch of the upward-propagating thermal and moves upwards with the thermal. This region is separate from the low-level downdraught, which is rain-induced.

The updraught and downdraught strengths in Experiments 5–7 are broadly similar and therefore insensitive to the background rotation rate (Table 2). This insensitivity is in contrast to the dependence on background rotation found in Wissmeier and Smith (2011) and is likely due to the smaller values of CIN in the present sounding. While CAPE values are broadly similar between the sounding in Wissmeier and Smith (2011) and the standard one used in this study (1800 J kg^{-1} compared with 2080 J kg^{-1}), the necessity of a 3.5 K thermal bubble to initiate convection in Wissmeier and Smith's study indicates that there is substantially more CIN present in their sounding.

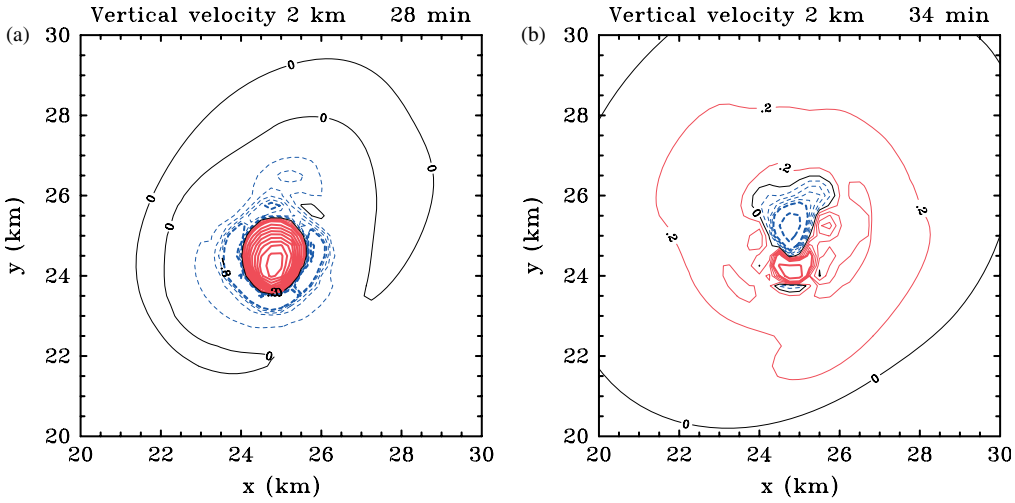

Figure 8. Horizontal cross-section of the vertical velocity at a height of 2 km in Experiment 5 at (a) 28 min and (b) 34 min. The former time is when the updraught at this level is a maximum, the latter time when the downdraught is a maximum. Contour interval: thin contours 0.2–0.8 m s^{-1}; thick contours 1 m s^{-1}. Solid (red) contours are positive, dashed (blue) contours negative. The thin black curve shows the zero contour. This figure is available in colour online at wileyonlinelibrary.com/journal/qj

With ice processes included, the updraught** and downdraught are stronger in Experiment 8 than in Experiment 5, with $w_{max} = 26.1$ m s^{-1}, compared with 23.8 m s^{-1}, and w_{min} at an altitude of 2 km equal to -4.4 m s^{-1}, compared with -2.9 m s^{-1}. The stronger updraught in the experiment with ice processes is due to the additional buoyancy provided by the latent heat of freezing and the stronger downdraught is due to the cooling associated with melting of falling ice particles.

6.2. *Relative vorticity*

The top panels of Figure 9 show vertical cross-sections of vertical velocity in the x–z and y–z planes and vertical vorticity in the x–z plane with rain water superimposed in Experiment 5 at 32 min. Figure 9(a) shows a relatively axisymmetric cell with the updraught maximum located near a height of 4 km. By this time a significant amount of rain water has formed within it, as seen by the co-location of the updraught maximum and the rain water maximum. The strongest downdraught at this time occurs in an annular region around the updraught core at a height of about 4 km. This downdraught is part of the subsiding branch of the upward-propagating thermal, as noted previously in reference to Figure 8. Figure 9(b) shows a slice through the middle of Figure 9(a). In this plane, the effects of the vertical wind shear are evident in the tilt of the updraught with height towards the y-direction.

The vorticity profile in the x–z cross-section (Figure 9(c)) is slightly asymmetric about the domain centre and has an inner dipole structure with cyclonic vorticity to the right and a weaker dipole structure outside it with cyclonic vorticity to the left. To understand this structure, we note that the buoyancy of the rising thermal creates toroidal vorticity, which, together with ambient horizontal and vertical vorticity, is tilted by the horizontal gradient of vertical velocity and stretched by the vertical gradient thereof. The tilting effect is not symmetric, as the toroidal vorticity, which is related largely to the horizontal gradient of vertical velocity, is not symmetric about the ordinate, having stronger values to the left in this case. This non-symmetric toroidal vorticity generation explains why the vertical vorticity *minimum* at a height of 4 km is larger in magnitude than the vertical vorticity maximum, when intuition might suggest that the latter quantity should be larger because of the presence of *cyclonic* background vorticity.

Figure 9(d) and (e) show horizontal cross-sections of vertical vorticity, vertical velocity and the horizontal wind structure at a height of 4 km in Experiment 5 at 30 and 32 min. Figure 9(d) shows the moment that the updraught reaches a height of 4 km, with the horizontal winds diverging outwards. The non-symmetric vorticity features are evident, as the positive vorticity anomaly is stronger in magnitude on the left of the updraught. By 32 min (Figure 9(e)) there is a significant difference, as a vorticity dipole (generated by the updraught as it tilts the background vorticity) becomes the main vortical structure. An annular downdraught region is apparent and the horizontal wind field is now convergent towards the updraught centre.

Figure 10 shows horizontal cross-sections of the vertical component of relative vorticity at a height of 500 m in Experiments 5–8 after 20, 44 and 60 min of integration. Superimposed on these cross-sections are the contours of vertical motion with magnitude greater than 1 m s^{-1}, where they exist. Prominent updraughts (vertical velocity > 1 m s^{-1}) at this level are delineated by a thick solid black contour and prominent downdraughts (vertical velocity < -1 m s^{-1}) are delineated by a thick black dashed contour. Unlike the corresponding patterns of vertical velocity and unlike the vorticity fields in Wissmeier and Smith's experiments, the vorticity fields are far from axisymmetric, mostly having a prominent dipole or quadrupole structure. The dipole features at 20 min (upper panels of Figure 10) are clearly a result of the tilting of horizontal vorticity associated with the background shear into the vertical by the updraught of the first convective cell, which is located over the centre of the vorticity dipole. Note that tilting acting alone would produce positive and negative vorticity anomalies of equal strength, whereas the additional effect here of the stretching of ambient cyclonic vertical vorticity leads to a stronger cyclonic gyre.

At later times (middle and lower panels of Figure 10), the vorticity fields have a quadrupole-like structure comprising a pair of dipoles. Animations of the fields show that the lower dipole constitutes the remnant vorticity that was formed by the first convective cell, while the upper dipole has formed by the tilting of background horizontal vorticity by the downdraught. Note that the downdraught occurs ahead of the tilted updraught in the y-direction (Figure 8(b)). At 44 min, the downdraught is co-located with the upper vertical vorticity dipole, while the updraught at the height of the cross-section has all but decayed (in Experiment 5 it had already decayed at low levels by 32 min: see Figure 9(a) and (b)). As the background rotation rate is increased in Experiments 5–7, the two positive vorticity anomalies are enhanced by the stretching of background cyclonic vorticity and

**The perceptive reader will notice that w_{max} at an altitude of 2 km is 2 m s^{-1} larger when ice processes are included, although at this stage no ice has formed! We traced this feature to the fact that the Gilmore ice scheme uses a different formulation of warm rain processes in Bryan's model from that in the scheme for warm rain only. Since it is unclear which warm-rain scheme is most accurate, we have not sought to implement one common scheme, but caution that this difference will affect the updraught magnitude.

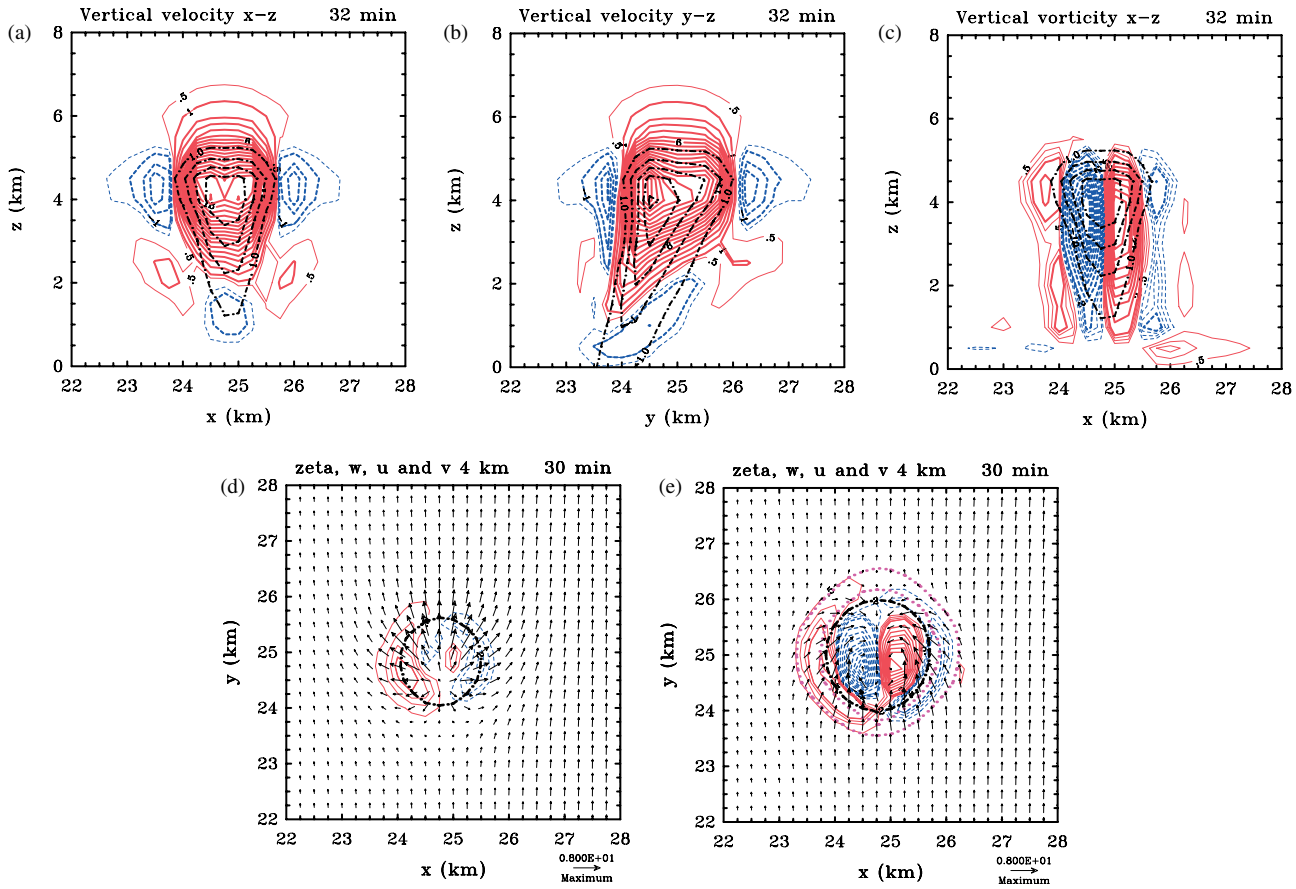

Figure 9. Panels (a) and (b) show vertical cross-sections (x–z and y–z) of vertical velocity, with contours of cloud water mixing ratio, through the centre of the domain at 32 min for Experiment 5, where the cell is located at this time. Panel (c) shows a vertical cross-section (x–z) of vertical vorticity, with contours of cloud water mixing ratio, through the centre of the domain at 32 min for Experiment 5. Contour interval: vertical velocity thin contour 0.5 m s^{-1}, thick contours 1 m s^{-1}; vertical vorticity thin contour 5×10^{-4} s^{-1}, thick contours 1×10^{-3} s^{-1}. Solid (red) contours are positive, dashed (blue) contours negative. Rain water contours: 1 g kg^{-1} in dot–dashed (black) contours. The lower panels show horizontal cross-sections of vertical vorticity, vertical velocity and horizontal winds at a height of 4 km at 30 and 32 min for Experiment 5. Contour interval: vertical vorticity thin contours 5×10^{-4} s^{-1} to 1.5×10^{-3} s^{-1}; thick contours 2×10^{-3} s^{-1}. Solid (red) contours are positive, dashed (blue) contours negative. Vertical velocity: thick contour 2 m s^{-1}, dot–dashed (black) contours positive, dotted (pink) contours negative. Surface wind vectors are relative to the maximum vector at the bottom right of panels (d) and (e). This figure is available in colour online at wileyonlinelibrary.com/journal/qj

subsequently merge to form a single elongated anomaly (three left middle panels of Figure 10). At 60 min, the two dipole pairs remain in all four experiments (lower panels of Figure 10).

In the simulations of Wissmeier and Smith (2011) and Kilroy and Smith (2012), the maximum amplification of vertical vorticity occurs near the surface and is associated with stretching of vertical vorticity by the vertical gradient of the updraught mass flux. At early times the latter is large and positive near the surface because the buoyancy of the initial thermal is a maximum there. In Experiments 1–3 of Kilroy and Smith (2012), there was little or no amplification of vorticity above a height of 5 km. Their results show that, in a non-sheared environment containing ambient background rotation, the maximum amplification occurs close to the surface. In the current study, in the presence of vertical shear, tilting plays a large role in vorticity generation and increases the depth to which significant vorticity anomalies occur.

Details of the vorticity maxima and minima at selected heights for Experiments 5–8 are included in Table 3. As the background rotation rate is increased from zero in Experiment 5 to ζ_0 in Experiment 7, ζ_{max} increases, while the magnitude of $\zeta 1_{min}$ and $\zeta 4_{min}$ decrease (Table 3). The low-level vorticity, characterized for example by $\zeta 1_{max}$, increases from 1.2×10^{-2} s^{-1} to 1.8×10^{-2} s^{-1}, whereas the magnitude of $\zeta 1_{min}$ decreases from 1.2×10^{-2} s^{-1} to 8.2×10^{-3} s^{-1}. The increase in $\zeta 0.5_{max}$ is even larger than $\zeta 1_{max}$ as the rotation rate is increased. Thus, at low levels, where the stretching of background vorticity is largest, cyclonic vorticity anomalies are increased in magnitude while anticyclonic anomalies are decreased. At a height of 4 km there is little change in the magnitude of the cyclonic vorticity anomalies as the background rotation increases, implying that the largest contribution to cyclonic vertical vorticity is by tilting at these levels. Interestingly, the maximum anticyclonic vorticity anomaly at a height of 4 km is largest when there is no background rotation and weakens slightly with increasing rotation. As explained above, this behaviour is due to the non-symmetric horizontal vorticity structure produced by the sheared thermal as it generates toroidal vorticity. Our finding that the negative vorticity anomaly is larger in magnitude than the positive anomaly may not be a general result and may be related to the particular signs of the background horizontal and vertical shear in our experiments.

At least in the absence of background rotation, the inclusion of ice microphysics has little impact on the amplification of low-level vorticity. For example, $\zeta 0.5_{max}$ and $\zeta 1_{max}$ have values of 1.1 and 1.2×10^{-2} s^{-1} in Experiment 8, compared with 8.6 and 1.2×10^{-2} s^{-1}, respectively, in Experiment 5. This finding is consistent with the fact that the inclusion of ice microphysics leads to additional buoyancy only above the freezing level (i.e. above a height of 5 km).

Figure 11 shows time–height cross-sections of the maximum vertical vorticity in Experiments 5–8 and the minimum vertical vorticity in Experiments 5 and 8 (recall footnote in section 3). Features to notice are that there is a significant generation of vertical vorticity to heights of 5–8 km in the experiments with warm rain only (Experiments 5–7) and up to 10 km in the experiment with ice microphysics (Experiment 8). Another significant feature is that, as the background rotation rate increases, there is a marked increase in the magnitude of low-level vertical vorticity, as discussed previously (Figure 11(a)–(c)). There is an increase also in the magnitude of vertical vorticity located near a height of 4 km, as the background rotation rate increases. In contrast, the vorticity anomaly located at a height of 6 km weakens earlier as the background rotation rate increases.

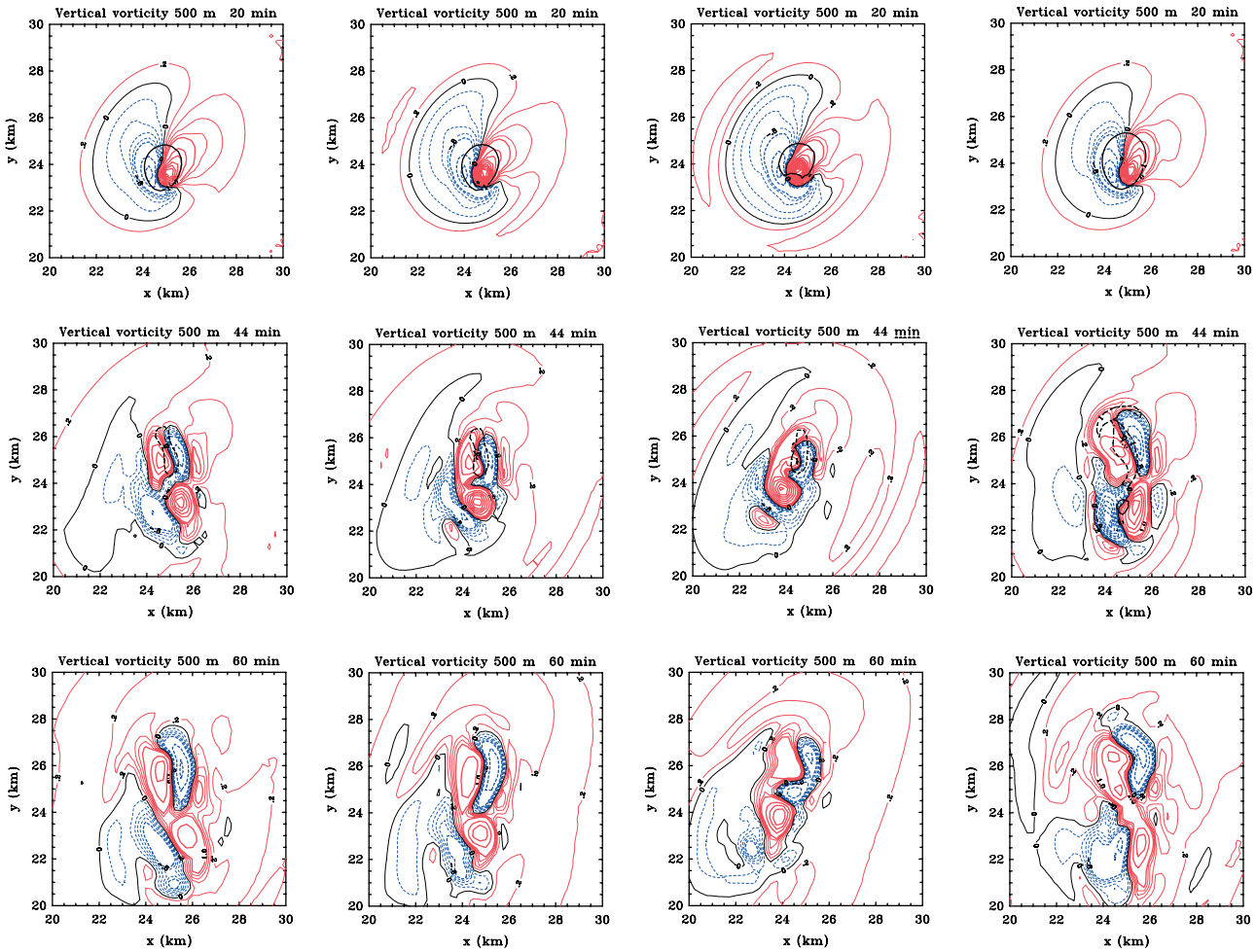

Figure 10. Horizontal cross-section of the vertical component of relative vorticity at 20 min (upper panels), 44 min (middle panels) and 60 min (lower panels) at a height of 500 m in the four experiments: from left to right Experiments 5, 6, 7 and 8. Contour interval: thin contours $2 \times 10^{-4}\,s^{-1}$ to $8 \times 10^{-4}\,s^{-1}$; thick contours $1 \times 10^{-3}\,s^{-1}$. Solid (red) contours are positive, dashed (blue) contours negative. The thin black curve shows the zero contour. The thick black contours show the $1\,m\,s^{-1}$ (solid) and $-1\,m\,s^{-1}$ (dashed) contour of vertical velocity. This figure is available in colour online at wileyonlinelibrary.com/journal/qj

A small patch of vorticity located above a height of 8 km in Figure 11(b) and (c) is due to the stretching of background vertical vorticity by gravity waves generated by the updraught.

While the inclusion of ice processes has little effect on the generation of vorticity at low levels, there is a significant effect on middle tropospheric vorticity enhancement (compare Figure 11(a) and (d)). The vorticity maxima are mostly comparable between Experiments 5 and 8, but the region of enhanced vorticity in Experiment 8 extends through a larger depth and persists longer than in the warm rain experiment. Again, this finding is consistent with the fact that the inclusion of ice microphysics leads to additional buoyancy only above the freezing level.

In summary, at early times the convection produced in Experiments 5–8 has a prominent vorticity dipole structure associated with the tilting of ambient horizontal vorticity by the updraught. At later times a second vorticity dipole forms ahead of the slanted updraught through the tilting of ambient vorticity by the convective downdraught. The strength of the cyclonic vertical vorticity anomalies increases at low levels as the background rotation rate increases because of the increased stretching of ambient cyclonic vertical vorticity. In fact, the vorticity maximum in the experiment with the largest background rotation rate is located at the surface. At mid-levels there is little change in the magnitude of the vorticity maxima as the background rotation increases, implying that the largest contribution to vertical vorticity is by tilting at these levels. In the presence of background vertical shear, tilting plays an important role in vertical vorticity generation and increases the depth to which significant vorticity anomalies occur. In contrast, in similar calculations without vertical shear, there is no appreciable amplification of vorticity above a height of 5 km.

The inclusion of ice microphysics increases the updraught and downdraught strength as expected and provides a much deeper area of enhanced vorticity that persists longer than in the warm rain experiment.

7. Updraught splitting in combined horizontal and vertical shear

We consider now updraught splitting in a background flow with both horizontal and vertical shear in a configuration similar to that in the previous section, but without background rotation. The next two experiments are guided by the results of sections 4 and 5, which showed that splitting is favoured by relatively unstable soundings and relatively large low-level vertical shear. In these experiments we increase the amount of low-level shear in the standard wind profile (shown in Figure 2) and use the unstable sounding. We perform first an experiment with no horizontal shear (Experiment 9). This experiment differs from Experiments 2 and 3 in that the background wind becomes effectively constant with height above about 2 km, a necessary simplification in order to interpret the results more easily. Experiment 10 is a repeat of Experiment 9 with horizontal shear included. In both experiments the increased low-level vertical shear is achieved by trebling the value of b in Eq. (3).

Table 2 shows the maximum updraught and downdraught strengths at various heights for these experiments. The larger maximum vertical velocity occurs in the experiment with horizontal shear ($21.6\,m\,s^{-1}$ compared with $18.7\,m\,s^{-1}$). The domain maximum updraught velocities listed in Table 2 for

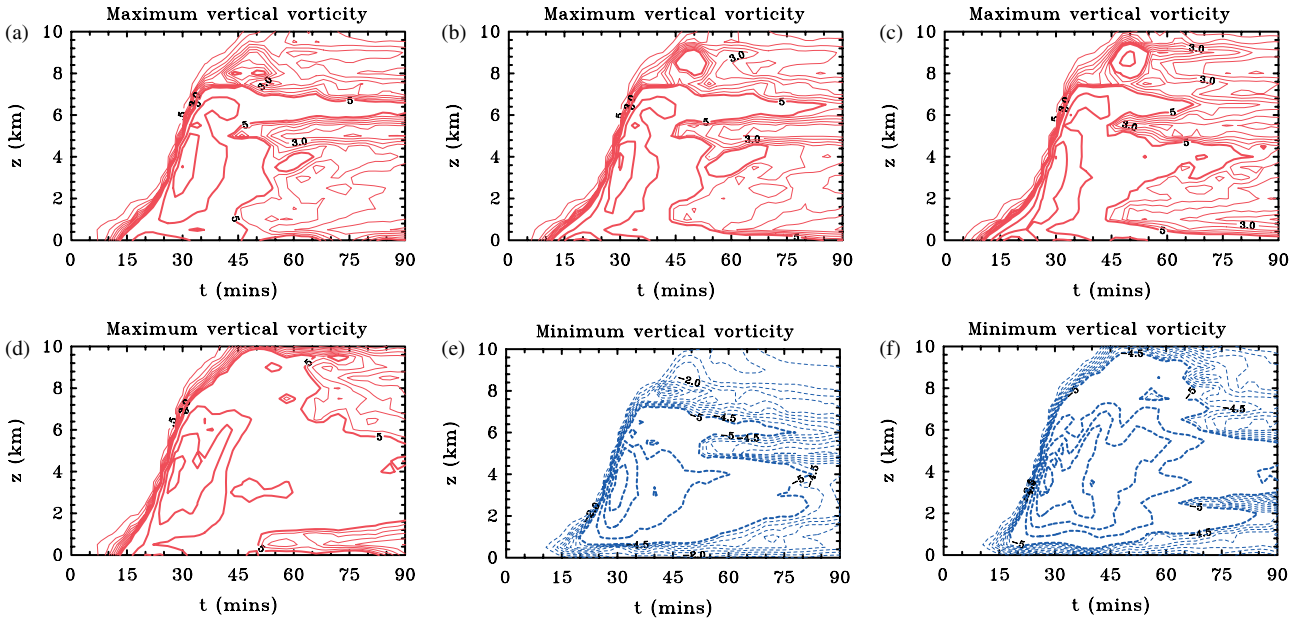

Figure 11. Time–height series of maximum vertical vorticity in four experiments: (a) Experiment 5, (b) Experiment 6, (c) Experiment 7 and (d) Experiment 8, together with the minimum vertical vorticity in (e) Experiment 5 and (f) Experiment 8. Contour interval: thin contours 0.5–4.5 $\times$ 10^{-3} s^{-1}; thick contours 5 $\times$ 10^{-3} s^{-1}. Solid (red) contours are positive, dashed (blue) contours negative. This figure is available in colour online at wileyonlinelibrary.com/journal/qj

Experiment 10 occur late in the simulation (after 100 min), while some of the values for Experiment 9 occur much sooner (after 50 min), indicating that the most vigorous convection occurs later in the presence of horizontal shear. While the maximum downdraught velocities are largely comparable in the two experiments, it is interesting to note that both these experiments contain the strongest downdraughts found in this study at a height of 2 km. These strong downdraughts account for the ease with which new cells develop along the gust front and, therefore, for the complexity of the vorticity structure at later times.

Experiments 9 and 10 have maximum vertical vorticities of 3.5 and 3.8 $\times$ 10^{-2} s^{-1}, respectively (Table 3). The maximum found in Experiment 9 occurs at a height of 1.5 km, which is in contrast to the finding of the previous unidirectional vertical shear experiments. (Recall that in Experiments 2 and 3 the vertical vorticity maxima are found at heights of 6 and 8 km, respectively.) The vorticity maximum at low levels in Experiment 9 is a result of using the standard wind profile, which has no vertical shear above a height of 2 km, so that there is little contribution to vorticity production by tilting much above this height.

Figure 12 shows horizontal cross-sections of the vertical component of relative vorticity at a height of 4 km for Experiments 9 and 10 at selected times. Also shown is the 2 m s^{-1} contour of vertical velocity, which is used to determine whether updraught splitting has occurred. In the presence of vertical shear only (Figure 12(a)–(d)), the vorticity features remain symmetric about the ordinate throughout the simulation. At 30 and 44 min, the pattern is dominated by an inner dipole associated with the tilting of horizontal vorticity by the updraught of the rising thermal and by an outer dipole, opposite in sign, on the flanks of the updraught, which is associated with the tilting of vorticity by the downward motion there. A split in the updraught has begun to appear as early as 44 min at this level. At 70 min, a complete split has occurred, with a distance of nearly 5 km separating the two most prominent updraughts. At 80 min, the vorticity pattern is more complex, reflecting the development of additional convective cells.

When horizontal shear is included, the vorticity pattern is again approximately symmetric about the ordinate at 30 min (Figure 12(e)), although a slight distortion by the horizontal shear is evident. However, even at 44 min, the symmetry has become lost and, as in Experiment 9, the updraught has started to split at this level. By this time, an intense cyclonic vorticity anomaly has developed in the upper half of the domain (Figure 12(f)). Vertical cross-sections in the x- and y-directions through the vorticity maximum in Figure 12(f) (not shown) indicate that this feature is associated with an updraught–downdraught couplet that breaks off from the main updraught cell, generating cyclonic vertical vorticity between the updraught and downdraught, presumably by stretching. This updraught–downdraught couplet decays rapidly, but the vorticity signature decays less rapidly. This process is repeated several times before the end of the calculation. The vertical vorticity on the flanks of the main dipole, associated with the subsiding part of the thermal, has a stronger cyclonic anomaly and a weaker anticyclonic one than in Experiment 9 (Figure 12(b) and (f)).

The subsequent evolution of the vorticity field is different from that in Experiment 9, even before splitting occurs at around 70 min. At this time the updraught that is co-located with the anticyclonic vorticity anomaly is noticeably filamented and has wrapped around the cyclonic vorticity patch associated with the overturning thermal (see Figure 12(g)). The vorticity features are predominantly cyclonic on the right side of the domain and predominantly anticyclonic on the left side. By 80 min, there is a large coherent patch of cyclonic vorticity with little updraught signature in the upper part of the domain. This feature is a manifestation of the successive vorticity generated by the 'cut-off' updraught–downdraught couplets as described above. The updraught centre located to the right of the domain has evolved from the updraught on the right of the first split cell and contains anticyclonic vorticity associated with tilting of background horizontal vorticity. In both experiments, new convective cells have formed along the spreading gust front and have generated new vorticity dipoles on both right and left sides of the domain.

8. Conclusions

We have described a series of numerical experiments designed to isolate the effects of ambient wind shear, both horizontal and vertical, on the generation of vertical vorticity by deep convection in tropical depressions. The first set of experiments quantifies the effect of a unidirectional boundary-layer-type wind profile on vorticity generation. The implementation of such a profile has a dramatic effect on convection, markedly weakening convective updraughts and downdraughts, thereby reducing the amplification of vertical vorticity and lowering the height to which updraughts penetrate. In the boundary-layer-type wind

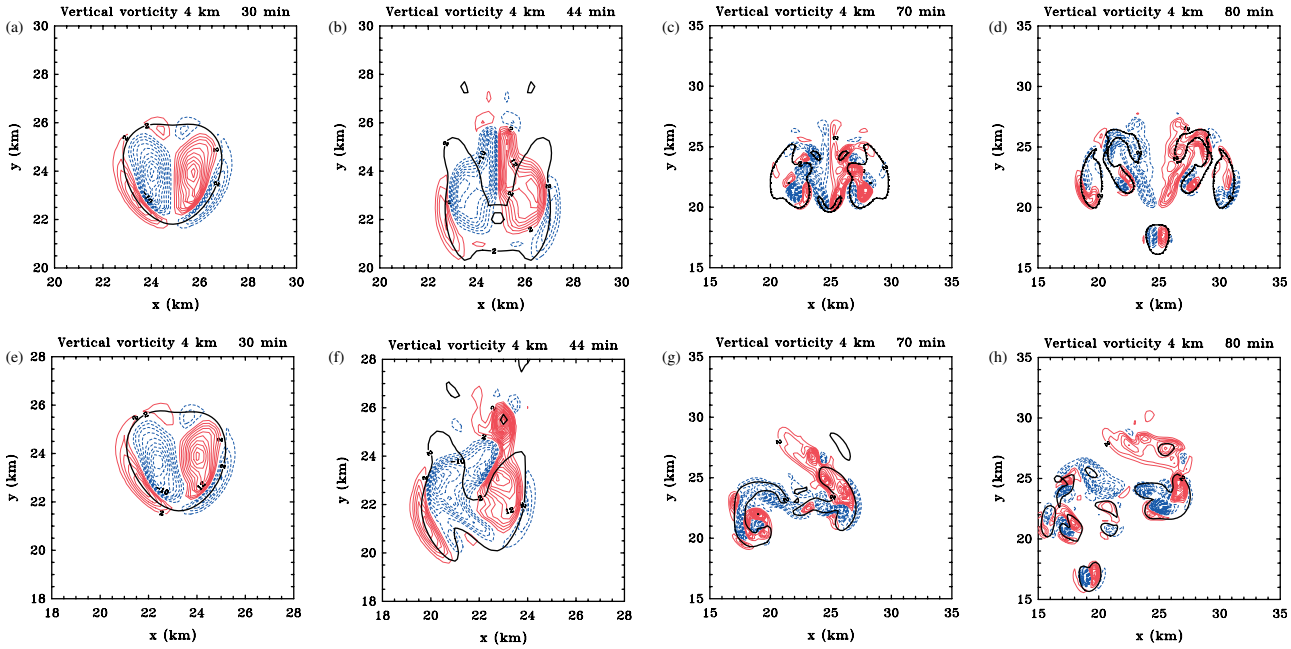

Figure 12. Horizontal cross-section of the vertical component of relative vorticity for Experiment 9 (upper panels) and Experiment 10 (lower panels) at four different times: from left to right 30, 44, 70 and 80 min. Contour interval: thick contours 2×10^{-3} s^{-1}. Solid (red) contours are positive, dashed (blue) contours negative. The thick black curve shows the 2 m s^{-1} contour of vertical velocity. Note that it is necessary to use a larger domain in plots showing 70 and 80 min to show all the necessary convective features. This figure is available in colour online at wileyonlinelibrary.com/journal/qj

simulation, the weakening results largely from the deformation of the initial bubble by low-level vertical shear. This bubble rises first through a layer of positive vertical shear and subsequently through one of negative vertical shear, so that the sign of the background horizontal vorticity it experiences reverses. Thus, two oppositely signed vorticity dipoles emerge within the updraught, one in the layer of positive vertical wind shear and the other in the layer of negative vertical wind shear. This finding introduces an element of complication in interpretations of the merger of convectively induced cyclonic vorticity anomalies in terms of barotropic dynamics.

Two experiments were carried out to quantify the effect that storm splitting has on vorticity generation, one in a purely vertically sheared environment and one in a purely horizontally sheared environment. In the experiment with pure vertical shear, the maximum vertical velocity and vorticity occur after storm splitting. However, in the experiment with pure horizontal shear, the maximum values of vertical velocity and low-level vertical vorticity occur before splitting. In this experiment, a large patch of anticyclonic vertical vorticity is generated despite there being no background source of horizontal vorticity or negative vertical vorticity. This feature may be attributed to the spreading cold pool, which generates horizontal vorticity. This horizontal vorticity is subsequently tilted into the vertical by the split updraughts.

Three experiments were carried out to examine the effects of adding background rotation to the standard boundary-layer-type wind shear profile. The convection produced has a prominent vorticity dipole associated with the tilting of horizontal vorticity. A second oppositely signed dipole is produced at later times, generated by the tilting of ambient horizontal vorticity by the convective *downdraught*. As the background rotation rate increases, so does the strength of the positive low-level vertical vorticity anomalies. However, there is little effect on the strength of those in the middle troposphere, indicating that the largest contribution to vertical vorticity production at these levels is by tilting.

The inclusion of ice microphysics increases the updraught and downdraught strengths and leads also to a much deeper layer of amplified vorticity than in the warm rain experiment and one that persists for longer.

Finally, two experiments were carried out to examine vorticity generation in the case of storm splitting in a combined horizontal and low-level vertical shear environment. In the presence of vertical shear only, the vorticity features remain symmetric about the direction of shear throughout the simulation, whereas horizontal shear destroys this symmetry and the evolution of the vorticity field becomes more complex, with new flanking cells continuously flaring up. Work is in progress to study the effects of more complex wind profiles with negative vertical shear aloft instead of a uniform flow and with a more realistic boundary-layer wind profile with low-level inflow. The results of this study will be reported in due course.

Acknowledgements

We thank Dr George Bryan for generously making the CM1 model available, as well as two anonymous reviewers for their perceptive and constructive comments on an earlier version of the manuscript. The research was supported by the German Research Council Grant: SM30/25-1.

References

Bao J-W, Gopalakrishnan SG, Michelson SA, Marks FD, Montgomery MT. 2012. Impact of physics representations in the HWRFX on simulated hurricane structure and pressure wind relationships. *Mon. Weather Rev.* **140**: 3278–3299.

Black PG. 1983. Tropical storm structure as revealed by stereoscopic photographs from Skylab. *Adv. Space Res.* **2**: 115–124.

Browning KA. 1964. Airflow and precipitation trajectories within severe local storms which travel to the right of the winds. *J. Atmos. Sci.* **21**: 634–639.

Bryan GH. 2002. '*An investigation of the convective region of numerically simulated squall lines*', PhD dissertation. The Pennsylvania State University: College Park, PA.

Bryan GH, Fritsch JM. 2002. A benchmark simulation for moist nonhydrostatic numerical models. *Mon. Weather Rev.* **130**: 2917–2928.

Cotton WR, Bryan GH, Van Den Heever SC. 2011. *Storm and Cloud Dynamics* (2nd edn). Academic Press: New York, NY.

Didlake AC, Houze RA. 2011. Kinematics of the secondary eyewall observed in Hurricane *Rita* (2005). *J. Atmos. Sci.* **68**: 1620–1636.

Douglas MW. 1992. Structure and dynamics of two monsoon depressions. Part II: Vorticity and heat budgets. *Mon. Weather Rev.* **120**: 1548–1564.

Dunion JP, Marron CS. 2008. A reexamination of the Jordan mean tropical sounding based on awareness of the Saharan Air Layer: Results from 2002. *J. Atmos. Sci.* **21**: 5242–5253.

Fang J, Zhang F. 2010. Initial development and genesis of Hurricane *Dolly* (2008). *J. Atmos. Sci.* **67**: 655–672.

Foster IJ, Lyons TJ, 1984. Tropical cyclogenesis: A comparative study of two depressions in the northwest of Australia. *Q. J. R. Meteorol. Soc.* **110**: 105–119.

Gentry RC, Fujita TT, Sheets RC. 1970. Aircraft, spacecraft, satellite and radar observations of Hurricane *Gladys*. *J. Appl. Meteorol.* **9**: 837–850.

Gilmore MS, Straka JM, Rasmussen EN. 2004. Precipitation and evolution sensitivity in simulated deep convective storms: Comparisons between liquid-only and simple ice and liquid phase microphysics. *Mon. Weather Rev.* **132**: 1897–1916.

Gopalakrishnan SG, Marks FD, Zhang X, Bao JW, Yeh K-S, Atlas R. 2011. The experimental HWRF system: A study on the influence of horizontal resolution on the structure and intensity changes in tropical cyclones using an idealized framework. *Mon. Weather Rev.* **139**: 1762–1784.

Hendricks EA, Montgomery MT, Davis CA. 2004. On the role of 'vortical' hot towers in formation of tropical cyclone *Diana* (1984). *J. Atmos. Sci.* **61**: 1209–1232.

Kilroy G, Smith RK. 2012. A numerical study of rotating convection during tropical cyclogenesis. *Q. J. R. Meteorol. Soc.* **139**: 1255–1269.

Lin YL, Farley RD, Orville HD. 1983. Bulk parameterization of the snow field in a cloud model. *J. Clim. Appl. Meteorol.* **22**: 1065–1092.

Montgomery MT, Nicholls ME, Cram TA, Saunders AB. 2006. A vortical hot tower route to tropical cyclogenesis. *J. Atmos. Sci.* **63**: 355–386.

Nguyen SV, Smith RK, Montgomery MT. 2008. Tropical-cyclone intensification and predictability in three dimensions. *Q. J. R. Meteorol. Soc.* **134**: 563–582.

Nguyen CM, Reeder MJ, Davidson NE, Smith RK, Montgomery MT. 2010. Inner-core vacillation cycles during the rapid intensification of Hurricane *Katrina*. *Q. J. R. Meteorol. Soc.* **137**: 829–844.

Persing J, Montgomery MT, McWilliams J, Smith RK. 2013. Asymmetric and axisymmetric dynamics of tropical cyclones. *Atmos. Chem. Phys.* **13**: 12299–12341.

Rotunno R, Klemp JB. 1982. The influence of the shear-induced pressure gradient on thunderstorm motion. *Mon. Weather Rev.* **110**: 136–151.

Rotunno R, Klemp JB. 1985. On the rotation and propagation of simulated supercell thunderstorms. *J. Atmos. Sci.* **42**: 271–292.

Rozoff CM. 2007. '*Aspects of moat formation in tropical cyclone eyewall replacement cycles*', PhD thesis. Colorado State University: Fort Collins, CO.

Schlesinger RE. 1978. A three-dimensional numerical model of an isolated thunderstorm: Part I. Comparative experiments for variable ambient wind shear. *J. Atmos. Sci.* **35**: 690–713.

Shin S, Smith RK. 2008. Tropical-cyclone intensification and predictability in a minimal three dimensional model. *Q. J. R. Meteorol. Soc.* **134**: 1661–1671.

Smith RK, Montgomery MT. 2012. Observations of the convective environment in developing and non-developing tropical disturbances. *Q. J. R. Meteorol. Soc.* **138**: 1721–1739.

Smith RK, Montgomery MT. 2013. On the existence of the logarithmic surface layer in hurricanes. *Q. J. R. Meteorol. Soc.*, doi: 10.1002/qj.2121.

Weisman ML, Klemp JB. 1982. The dependence of numerically simulated convective storms on vertical wind shear and buoyancy. *Mon. Weather Rev.* **110**: 504–520.

Weisman ML, Klemp JB. 1984. The structure and classification of numerically simulated convective storms in directionally varying wind shears. *Mon. Weather Rev.* **112**: 2479–2498.

Wilhelmson RB, Klemp JB. 1978. A numerical study of storm splitting that leads to long-lived storms. *J. Atmos. Sci.* **35**: 1974–1986.

Wilhelmson RB, Klemp JB. 1981. A three-dimensional numerical simulation of splitting severe storms on 3 April 1964. *J. Atmos. Sci.* **38**: 1581–1600.

Wissmeier U. 2009. '*The physics of tropical convection*', PhD dissertation. Ludwig-Maximilians University of Munich: Munich, Germany.

Wissmeier U, Smith RK. 2011. Tropical-cyclone convection: The effects of ambient vertical vorticity. *Q. J. R. Meteorol. Soc.* **137**: 845–857.

